Radiometric and Geometric Calibration of a Visible Spectral Electro-Optic "Fisheye" Camera Radiance Distribution System

KENNETH J. VOSS

Institute of Marine Resources, Scripps Institution of Oceanography, University of California, San Diego, La Jolla, California

GIUSEPPE ZIBORDI

Institute for the Study of Geophysical and Environmental Methodologies, National Council of Research, Modena, Italy

(Manuscript received 22 July 1988, in final form 27 December 1988)

ABSTRACT

Camera systems which measure a complete hemispherical field ("fisheye" lens systems), can be applied to the measurement of the radiance, but accurate radiometric and geometric calibrations are required to obtain absolute radiance data. The calibration procedure applied to an instrument built for spectral and geometrical radiance distribution measurements in the visible wavelength region (450–650 nm), based on an electro-optic fisheye camera system, is described and validated through comparison with a more standard radiometer.

1. Introduction

Methods for making measurements of the total sky radiance distribution, and total underwater radiance distribution can be used for many purposes: ground truth of satellite data, validation of radiative transfer models, determination of physical and optical properties such as absorption and scattering phase function. In many studies, such as auroral emissions (Babey et al. 1986), bidirectional reflectance properties (Deering and Eck 1987), sky and underwater visibility (Boileau and Gordon 1966; Tyler 1960), and radiative transfer (Smith 1974), measurements of either the total sky or underwater radiance distributions (or both) are required. These measurements have not been performed widely in the past, however, because of the difficulty in making accurate measurements with sufficient angular resolution in a time short enough to avoid changes in the distribution during data collection. Recent advances in solid state camera systems have opened up methods of collecting this type of data quickly and accurately. "Fisheye" optics cover a hemispherical field of view and, coupled with an electro-optic camera system, allow a hemisphere of the radiance distribution to be gathered in a single image. Thus measurement takes place rapidly in a single frame period which, with implementation of a filter changer mechanism, allows measurement at several spectral bands to be performed in a short time.

A system for spectral measurement of the underwater and sky radiance distribution (composed of two cameras to obtain the upwelling and downwelling underwater radiance, and a third camera to obtain the sky radiance at the surface) has been developed and successfully applied in field measurements (Voss 1989). Particular care has been devoted to the radiometric and geometric calibration of the system in order to obtain absolute radiance values.

In this paper, with reference to the electro-optic fisheye Radiance Distribution Camera System used in atmospheric measurements, the calibration procedure is described and validated through comparison of contemporaneous measurements taken with the instrument and with a more standard sky radiometer.

2. Description of the instrument

The electro-optic fisheye Radiance Distribution Camera System (RADS) consists of a fisheye lens, a filter changer assembly, and a solid state camera (GE 2509 CID). Figure 1 shows a schematic of this system.

A fisheye converter lens (Bicar) is used as input stage to the filter changer optics. This lens typically extends the field of view of a more conventional lens to allow a 2π solid angle in the object space to be projected onto the image plane. The filter changer optics are used to provide an appropriate optical path for light filtration and to enable image formation on the sensing device of the camera. The resultant optical system makes possible measurement of the radiance distribution from 0 to 87.5 degrees zenith and 360 degrees azimuth: almost an entire hemisphere.

The filter changer allows four spectral filters (to select desired spectral bands in the visible and near infrared regions) and four absorption neutral density filters (to

Corresponding author address: Dr. Kenneth Voss, Institute of Marine Resources/Scripps Institution of Oceanography, University of California, San Diego, Mail Code A-018, La Jolla, CA 92093.

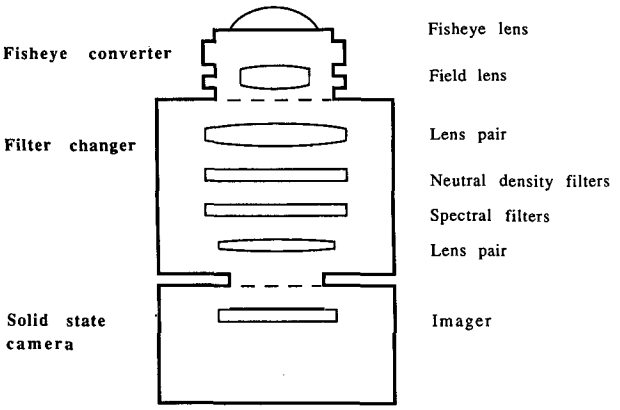

FIG. 1. A schematic of the electro-optics fisheye camera system.

adjust the overall scene dynamic range to the optimum camera level) to be inserted into the optical path of the instrument. The optical rays are not focused at the position occupied by the neutral density and spectral filters, so small spatial variations in the optical properties of the filters can be neglected. The maximum deviation of any ray from the optical axis of the camera system is 16 degrees, causing a maximum shift of 1.5% in the transmittance peak of the interference filters. The filter changer is remotely controlled allowing multiple spectral measurements in rapid succession to be performed.

The GE-2509 CID is a solid state camera with a Charge Injection Device (CID) imaging sensor, a resolution of 253 (vertical) × 260 (horizontal) elements, with the characteristics of low blooming [compared with Charge Coupled Devices (CCD) cameras (Sims and Denton 1987)], dynamic range of over two orders of magnitude, spectral responsivity between 400 and 1100 nm and frame period of approximately $\frac{1}{30}$ s. The camera can perform, through remote control, on-chip integration of the incident irradiance, making possible an extension of the lower limit of the camera sensitivity.

A frame grabber (Poynting 509) is used to convert the analog signal from the camera into eight bit digital form (256 grey levels). A microcomputer (Hewlett Packard 310C) is used for overall system control, data handling, processing and storage. A color CRT allows data to be displayed on screen as false color images, and a $\frac{1}{4}$" cartridge tape drive (Hewlett Packard 9144A) with a storage capacity of 182 megabytes data per cartridge is used for permanent archiving of data.

3. Calibration

The irradiance in the image plane of ideal optics is proportional to the radiance field in the object space (Slater 1980). Therefore, radiometric and geometric calibration factors can be applied to digitized data of the radiance field, obtained with the optical system, to compute absolute radiometric values and determine their absolute spatial location. The necessary factors for the calibration of data taken with RADS have been derived from measurements carried out in the laboratory. In the following subsections, a description and quantitative results are given for each step of the applied calibration procedure.

a. Linearity calibration

Response of the measuring system to input flux is determined by both the camera and frame grabber (uniformity of the imager in linearity and sensitivity, frame grabber linearity), so the system linearity must be calibrated as a unit, and substitution of one or the other part requires recalibration. To test the uniformity in response of the imager, it is required that the imager be uniformly illuminated during measurements. To this end, the lens and filter changer were removed from the camera and the imager was illuminated by diffuse, unfocused light from a plastic diffusing plate which was itself illuminated on the back side with a lamp. The lamp supply current was constantly monitored during measurements to avoid changes in irradiance due to variation in the output of the power source. The lamp was moved away from the diffusing plate in steps which were calibrated to cause a 0.1 logarithmic (1 dB) reduction in irradiance. Images were saved at each step and were used to determine the linearity from a relative intensity of 1.0 to 0.01 irradiance units.

The result of this calibration is shown in Fig. 2, where the logarithm of the digitized values are plotted versus the logarithm of the relative irradiance incident on the imager; this illustrates the very linear response of the system. The count values given in Fig. 2 were determined by a 100 × 100 element average taken from the center of the imager. Before sampling, a "dark frame" was subtracted off, pixel by pixel. This frame consisted of an average of 5 frames of the dark field (obtained with the camera completely obscured), and it was used to remove the dark noise due to thermal generation of charges (noise dependent on temperature and integration time), manufacturing defects in the elements of the imager (spatially dependent noise), and the read out process (random noise).

To test the uniformity in response of the imager, the images obtained for the linearity calibration were divided into 4 × 4 element segments, and linearity tests and response curves were determined for each subsample. The imager was found to be very uniform, with a total variation of 3% in linearity and sensitivity.

Because of the uniformity exhibited by the imager, and for simplicity of processing, the elements of the imager were considered to have a linearity response equal to that given by the central 100 × 100 elements. The error associated with this assumption is less than 3%. Thus the relative linearized radiance, L_l, is given by

$$L_l = b(\mathrm{DN} - \mathrm{D0})^m, \qquad (1)$$

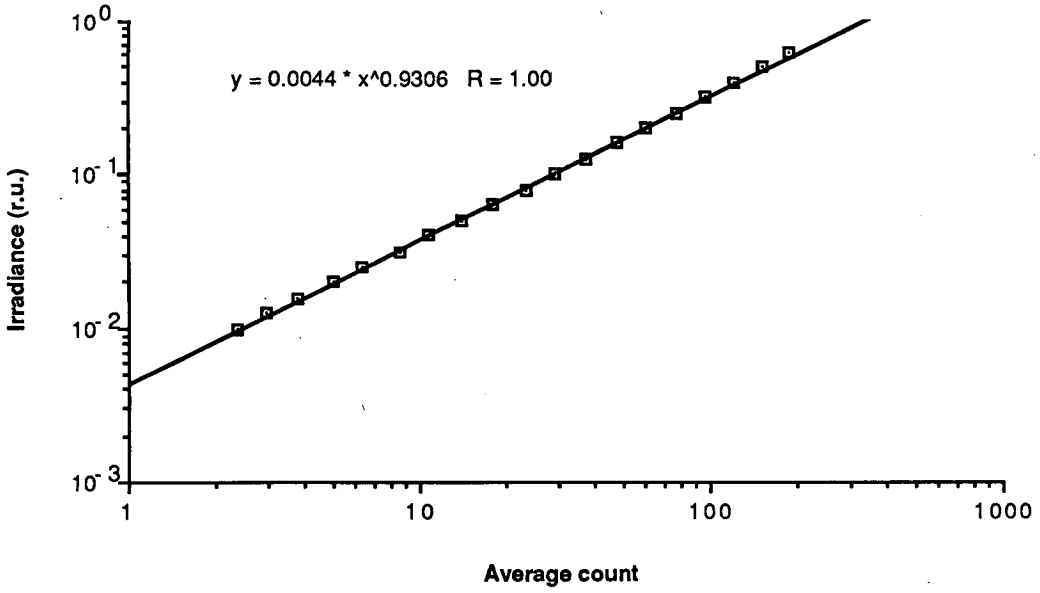

FIG. 2. Linearity of the system to input irradiance.

where DN is the digital number obtained from the irradiance measured by the analyzed element of the imager, D0 is the correspondent dark noise, and b (offset) and m (slope) are the coefficients derived from a logarithmic least-squares fit to digitized data of the relative irradiance measured by the imager (see Fig. 2).

b. *Spectral calibration*

Spectral calibration of the camera system was performed for each spectral filter in conjunction with the camera and lens response. The spectral response of the system is predominantly determined by the bandpass interference filters and to a lesser extent by the spectral sensitivity of the imager. The calibration was performed by illuminating the camera system with light from a monochromator. Images were obtained at 1 nm increments through the band pass of the system. From the average of a 3 × 3 subsample of the illuminated area the spectral characteristic of each channel were derived. Figure 3 shows the spectral response of the system and Table 1 lists the center wavelength and band pass for each channel.

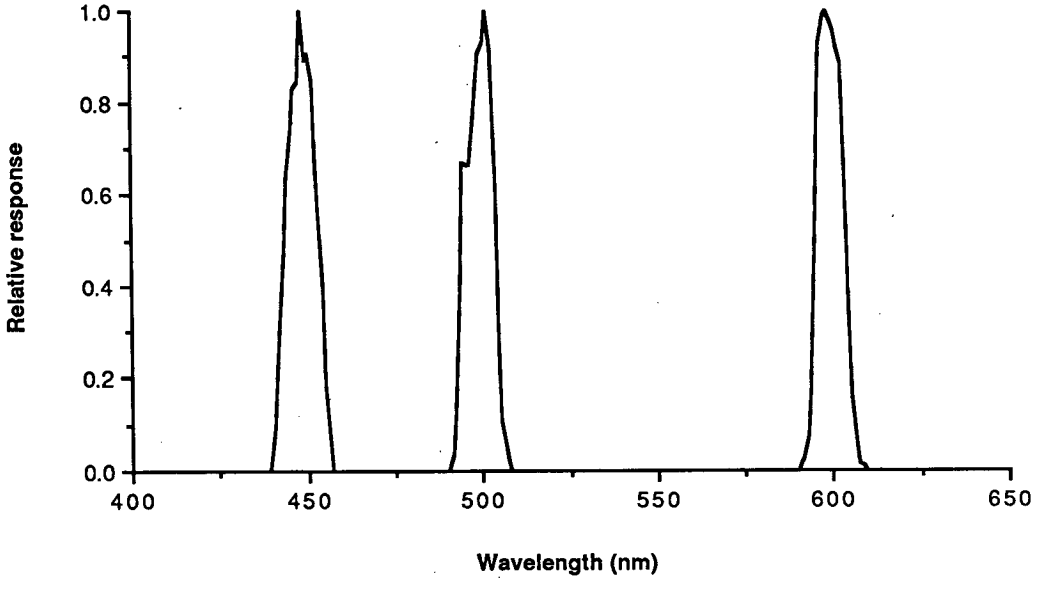

FIG. 3. Spectral response of the instrument; each filter response individually normalized.

TABLE 1. Spectral characteristics of the instrument.

Channel	Central wavelength (nm)	Bandwidth (nm)
1	449	10.5
2	499	10.0
3	600	9.5
4*	—	—

* Channel 4 was not implemented.

c. Geometric projection

The fisheye lens characteristically projects via an equidistant projection. For this type of lens

$$r = f\theta, \tag{2}$$

where r is the radial distance from the center on the image plane, f is the focal length of the lens system and θ is the view angle of the point source at infinity projected onto the image plane.

Geometric mapping of the radiance field onto the imager surface must be determined through calibration, thus checking the projection accuracy and experimentally evaluating f. To do this, the camera system was placed on a precision rotation mount at a distance over 3 meters from a small bright source (the source took up about 2 × 2 pixels in the image). The camera was rotated and images of the source were obtained at every 10 degrees. Figure 4 shows the result of this calibration step. These data prove that the optics exhibit a very linear projection, thus it follows an almost ideal equidistant projection. The derived f (given by slope of the curve in Fig. 4) allows view angles, θ, to be computed for each element of the imager through Eq. (2).

d. Rolloff

Rolloff of a lens (attenuation of radiance on increase in view angle) is an important aspect in the calibration of any imaging optical system. The optics of RADS is composed of the fisheye lens and a set of achromatic lenses in the filter changer. Theoretically, a fisheye lens following an equidistant projection (Miyamoto 1964) has a rolloff $R(\theta)$ given by

$$R(\theta) = \frac{\alpha \cos\theta(\sin\theta/\theta)}{f^2}, \tag{3}$$

where α is the area of the entrance aperture seen by the sensing element in the image plane and θ the view angle. Fisheye lenses have been built with the factor $\alpha \cos\theta$ nearly constant, in which case the rolloff is determined almost wholly by the $\sin\theta/\theta$ factor. But in general each fisheye lens design has its own inherent optical rolloff which must be determined through careful calibration. Conventional lenses exhibit a rolloff attenuation factor following a power of the cosine of the view angle (Slater 1980), so the general form for rolloff of the RADS optics may be given by

$$R(\theta) = \frac{\alpha \cos^n\theta(\sin\theta/\theta)}{f^2}. \tag{4}$$

To measure this factor, a barium sulfate plaque (of 20 cm diameter and exhibiting nearly lambertian characteristics) was placed approximately 100 cm from a standard calibration lamp, thus providing a stable, uniform radiance source. The plaque was viewed at approximately 45 degrees by the camera system which was placed on a rotating mount. Since the plaque-lamp geometry was not changed during measurements, the camera viewed a source of constant radiance. Images

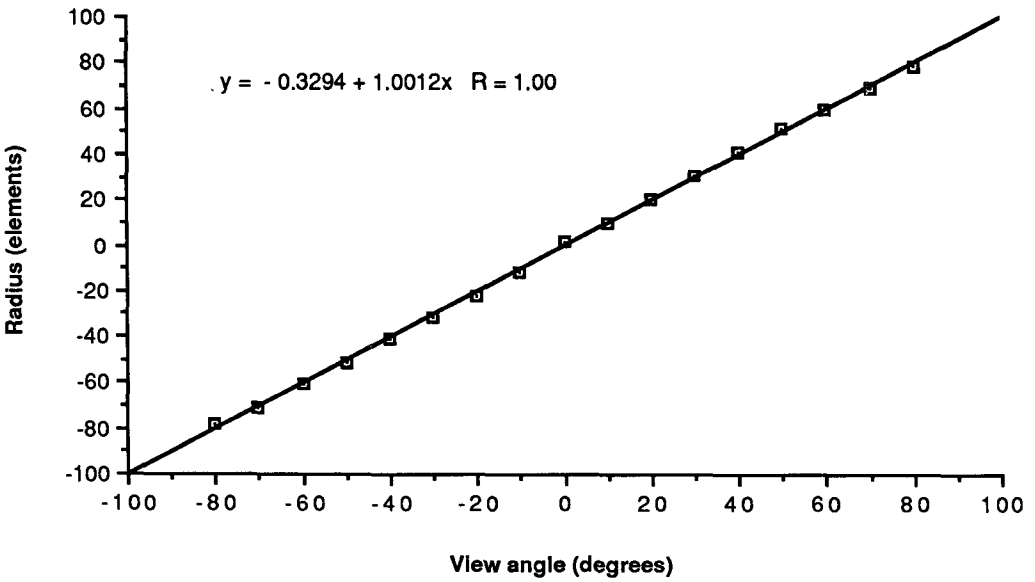

FIG. 4. Projection of the optics.

of the plaque were obtained at various view angles and investigated to determine the apparent rolloff of the optics system.

For calibration purposes a factor is desired which, when multiplied by the linearized radiance, will result in a rolloff corrected value. It was found that the rolloff, in our case, was best fit by a fifth order polynomial, in which all parameters appearing in Eq. (4) are accounted for. Figure 5 shows data obtained from measurements and the resulting curve fit used for rolloff correction.

The equation, derived from the fit, was found to reproduce the true optics rolloff within 2% (standard error of estimate resulting from fit was 1.8%). Tests were performed to determine the sensitivity of the rolloff correction to various factors, such as spectral bandpath, neutral density filters value and the mutual position of plaque and camera. No appreciable sensitivity to these factors has been discerned.

e. *Polarization sensitivity*

Sky light is polarized, and its polarization varies with direction, atmospheric conditions, and sun zenith angle (Plass and Kattawar 1970). The water radiance field is also polarized and its degree of polarization varies with depth and water optical properties (Waterman 1955). With a lens system the possibility of polarization sensitivity exists due to the fresnel coefficients at each surface of the lens. Polarization is therefore an important aspect in the performance analysis of a system designed to measure the radiance distribution of sky light, or the underwater radiance distributions.

To test the polarization sensitivity of RADS, the barium sulfate plaque was illuminated at approximately 60 degrees with an incandescent light source to provide an unpolarized radiance source. RADS was placed in a position to view the plaque, and a polarizer was inserted between the camera and the radiance plaque. Images were then obtained with different positions of the polarizer. RADS was also tilted with respect to the plaque, to enable measurement at various view angles (0, 15, 25, 45, 50, 70 degrees). The results of this test indicated that the camera does not have any significant polarization sensitivity. This implies that measurements of the radiance distribution with this system have negligible error due to polarization sensitivity.

f. *Absolute calibration*

To determine the absolute radiometric calibration factor, the barium sulfate plaque was illuminated at normal incidence with a 1000 W standard of spectral irradiance (calibration of which is traceable to National Bureau of Standards). The plaque was centered in the field of view of RADS at a distance of 50 cm from the lamp and viewed at 45 degrees.

The equation relating the irradiance $E(\lambda)$ incident on the plaque with the radiance $L(\lambda)$ reflected by the plaque (assuming a lambertian reflector) is

$$L(\lambda) = \rho \frac{E(\lambda)}{\pi}, \tag{5}$$

where ρ is the reflectance of the plaque (in this case, $\rho = 0.95$ with normal light incidence and 45 degrees viewing angle and it is almost constant in the spectral regions of interest).

Images of the plaque were obtained for each of the spectral filters, and the signal level counts were deter-

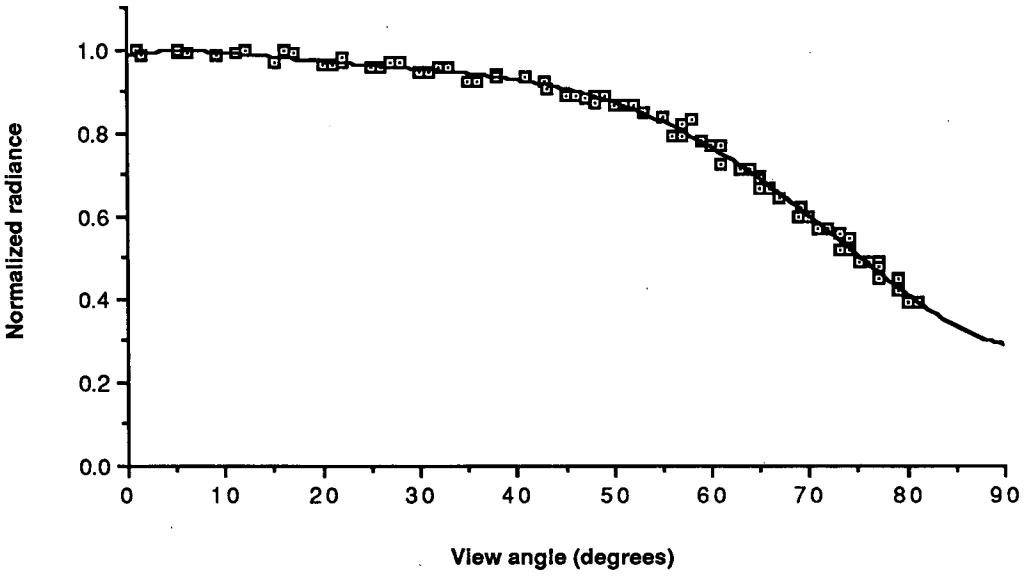

FIG. 5. Rolloff of the optics.

TABLE 2. Calibration constants.

Channel	$A(\lambda)$ (mW cm^{-2} μm^{-1} sr^{-1})	ND_1	ND_2	ND_3	ND_4
1	26.42	1.0	0.510	0.257	0.112
2	15.57	1.0	0.515	0.264	0.115
3	8.53	1.0	0.536	0.286	0.121
4*	—	—	—	—	—

* Channel 4 was not implemented.

mined from a 3 × 3 pixel area in the center of the plaque image. The absolute calibration factor $A(\lambda)$ was computed for each channel, dividing the plaque radiance by the average linearized value obtained from images:

$$A(\lambda) = \frac{L(\lambda)}{L_l}. \tag{6}$$

The possible errors in this factor are mainly caused by instabilities in the standard lamp irradiance, least count errors in the values obtained from the images (reduced by averaging pixels), and random noise in the imager. The error in the value of $A(\lambda)$ was found to be less than 5%, determined through multiple calibrations with two different standard lamps. In Table 2, the computed absolute calibration factors are given.

g. *Flare and blooming analysis*

To determine the flare and blooming characteristics of the camera lenses and imager, a simple test was performed. A helium neon laser was directed at the barium sulfate plaque that was imaged by the camera. The image of the laser beam subtended no more than one element on the sensor. No spill over to neighboring elements was detected with the imaged element saturated. In this manner the flare and blooming of the images were determined to be negligible (when reasonable care is taken to maintain the flux levels close to or below saturation).

h. *Neutral Density filters attenuation*

The attenuation values of the Neutral Density (ND) filters were determined by imaging the barium sulfate plaque through each neutral density filter (and with each spectral filter) and adjusting the signal level through use of the integration capability of the camera. The signal levels obtained from neighboring filters (ND1 and ND2, ND2 and ND3, and ND3 and ND4) were expressed as ratios and the attenuation value of each filter was determined by multiplying these ratios together. Measurements were taken with each spectral filter to account for wavelength dependence of the ND filters. The error in the final values are estimated to be less than 2%, with this error due to pixel to pixel variations in the mean used to determine the ratios. The computed data of the relative attenuation for each ND and spectral filter combination, are shown in Table 2.

i. *Injection Inhibit timing*

Photogenerated charge in solid state devices (such as CID or CCD), is linearly dependent on the integration time. RADS can perform, under remote control, on-chip integration of the incident irradiance through the use of the Injection Inhibit function of the camera. This function inhibits clearing of the imager between frame periods (the process of clearing is called "injection") so that the photogenerated charge is accumulated over several frame periods. Use of the Injection Inhibit function of the camera allows lower irradiance levels to be measured, but requires the determination of the inhibit time used in the function. This was determined by imaging a stable source repeatably with many different integration times (whose absolute value is determined by the Injection Inhibit time step: 1, 2, 3, . . .), determining the average of the response's intercept versus the Injection Inhibit time step, and comparing this value with the response for the basic integration period. In this system (camera and frame grabber) it was found an additional delay of 2.5 frame periods existed between the step of 1 and 2; for each additional increment above 2, each step corresponds to an additional frame period. Result of this analysis is shown in Fig. 6a.

The derived integration time I_t (frame periods) as a function of the Injection Inhibit time step I_s is given by

$$I_t = 1, \qquad (I_s = 1) \tag{7}$$

$$I_t = 2.5 + I_s, \quad (I_s > 1). \tag{8}$$

The applicability of the Injection Inhibit function is limited by the thermally generated dark noise and loses its usefulness when accumulation of charge due to thermally generated dark noise outstrips accumulation of light generated charge. Figure 6b illustrates the generation of dark noise as a function of the integration time at 25°C. Data have been obtained averaging 200 × 200 pixels in the center of the detected dark images, error bars give the standard deviation (less than 3.0 counts) of dark noise in the analyzed area.

j. *Final calibration factor*

The above factors taken together give the final calibration procedure of

$$L(\theta, \lambda) = (L_l - l_0)[A(\lambda)R(\theta)^{-1}\mathrm{ND}(\lambda)^{-1}I_t^{-1}], \tag{9}$$

where L_l is the linearized radiance in channel with central wavelength λ and computed through Eq. (1) for the output digital value of the considered element in the imager and l_0 accounts for variations in dark noise between calibration and field measurements.

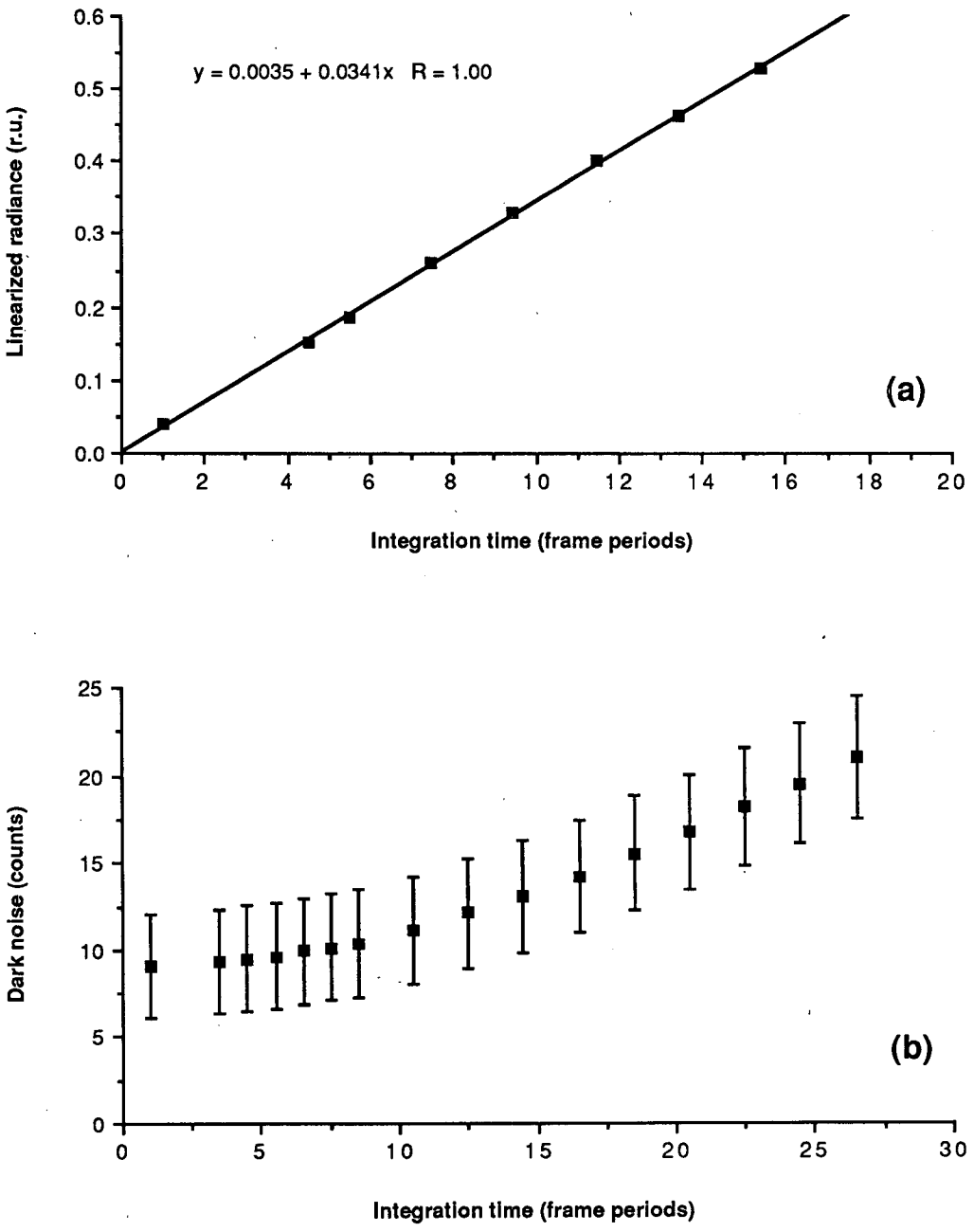

FIG. 6. Radiance (a) and dark noise (b) as a function of the integration time.

The dark noise D0, subtracted off the raw frame image in the linearization step, is obtained during calibration. In field measurements, variations in the dark noise of the imager can be caused by ambient temperature changes or use of different integration times or both. The term l_0 is obtained from an average linearized value of a sample of elements taken outside the projected image and accounts for the operational variations of the dark noise. So, while the dark field subtracted off pixel by pixel in the image during linearization removes the spatially dependent portion of the dark noise, l_0 accounts for temperature differences in the imager between the calibration and field use, and excess charge generated with increasing the integration time. This procedure has been validated by measurements showing no appreciable dependence on temperature or integration time in the spatially dependent contribution to dark noise.

The overall error in the RADS absolute calibration is less than 12% where the maximum relative error

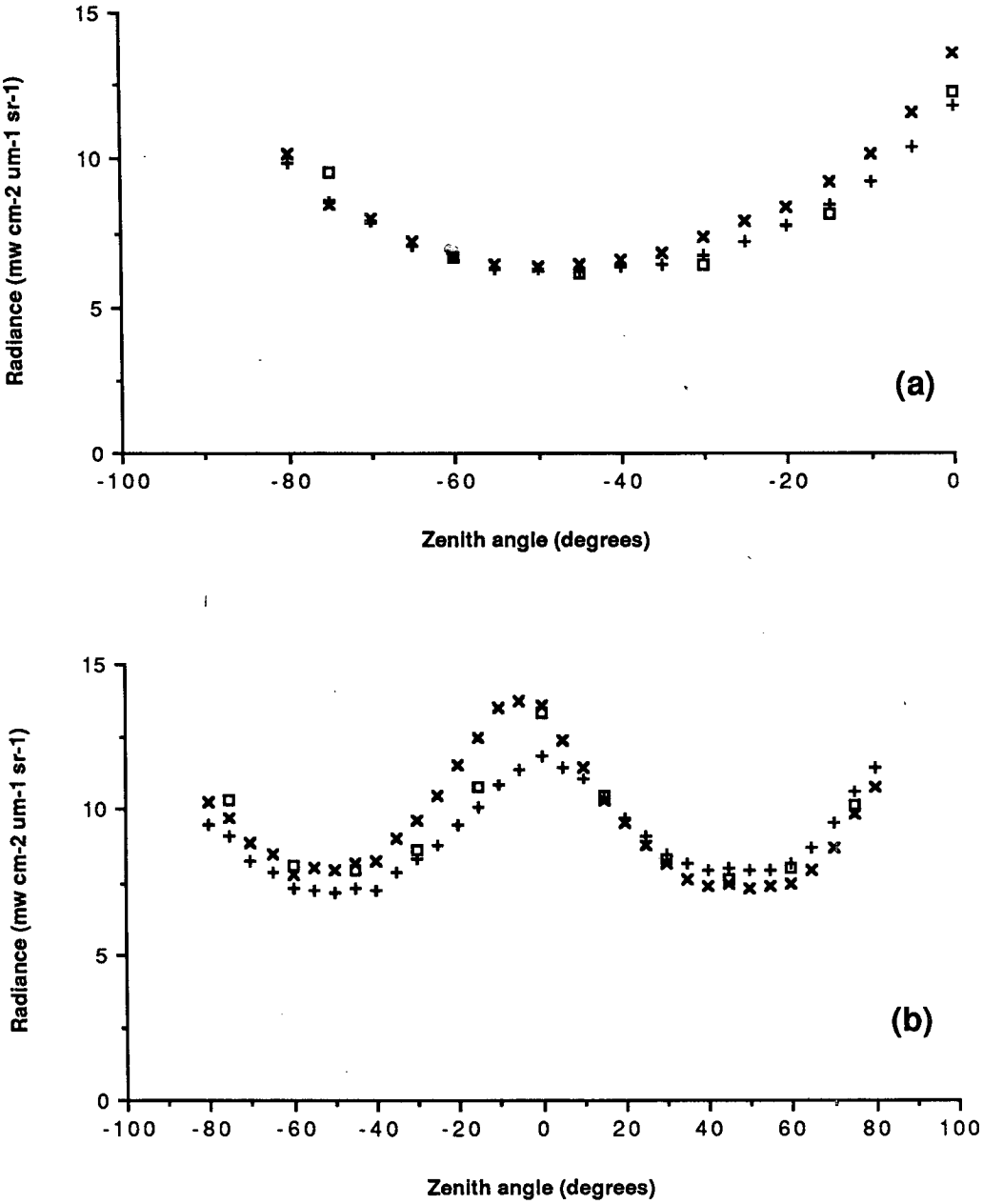

FIG. 7. Comparison between RADS data (×, +) and HHCRM data (□) taken at 449 nm and 441 nm central wavelengths respectively, in the sun plane (a) and in the sun-normal plane (b).

among data obtained from the same image is about 5% (due to methodologies applied in the linearization and rolloff correction).

4. Comparison with HHCRM data

a. Description of the experiment

On 13 May 1988 clear sky field measurements were obtained with RADS, and the Hand Held Contrast Reduction Meter (HHCRM). The HHCRM (Wilson 1979) is a gershun tube type radiometer with a 1 degree field of view and 10 spectral filters (10 nm wide) centered in the visible spectrum. This instrument was installed on an alta-azimuth mount to perform measurement of the sky radiance for selected angles in relation to the sun zenith plane. Measurements with the HHCRM (with error in absolute value within 4%) were performed at channels with central wavelength 441, 490 and 611 nm (close to the central wavelengths of RADS), at every 15 degrees in sky planes passing through the zenith. Before and after these measure-

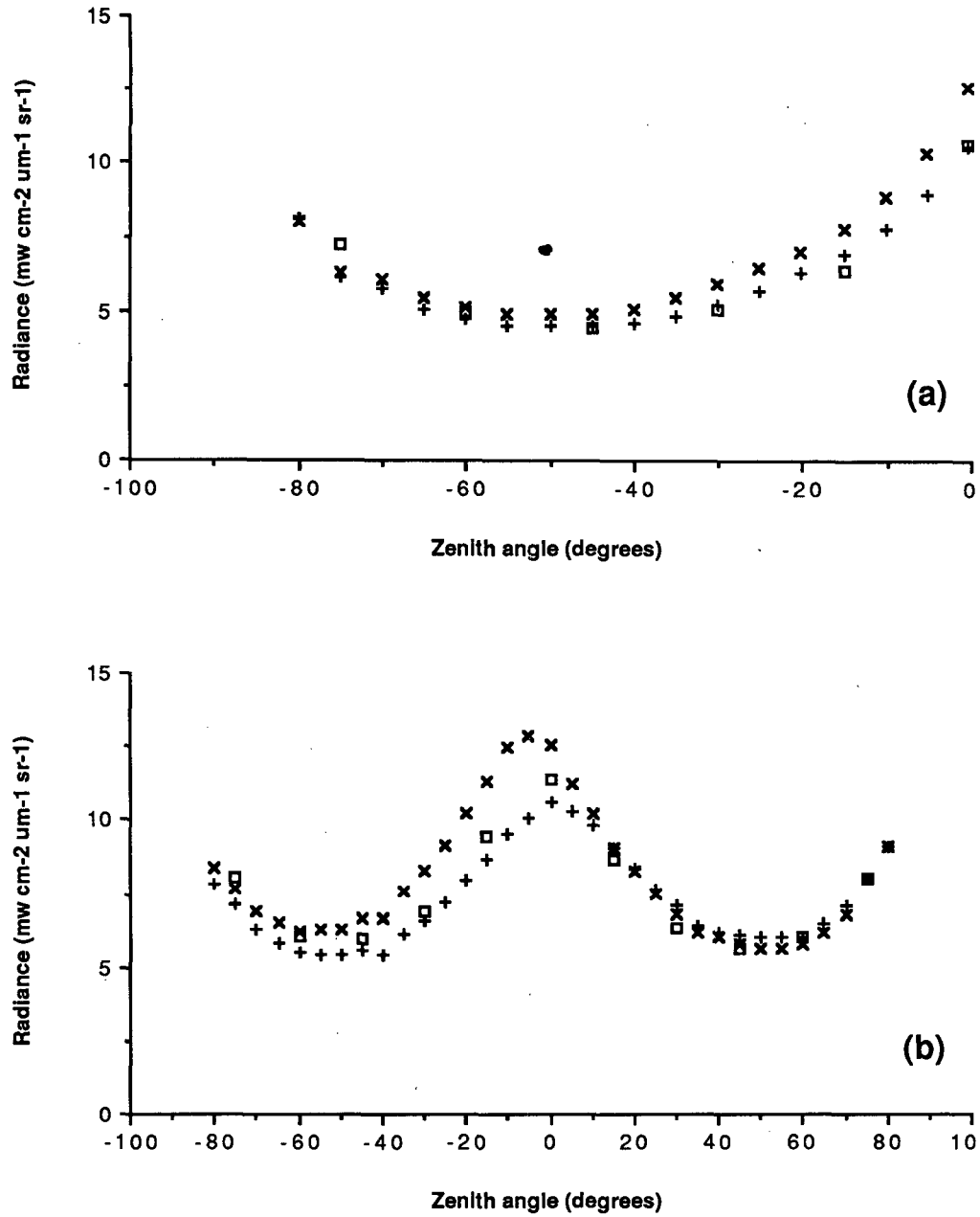

FIG. 8. Comparison between RADS data (×, +) and HHCRM data (□) taken at 499 nm and 490 nm central wavelengths respectively, in the sun plane (a) and in the sun-normal plane (b).

ments, an image was acquired and stored for each channel of RADS.

b. Data and discussion

Qualitative comparisons (because of the different central wavelengths) have been performed, between the radiance data derived from the HHCRM and RADS, to show the capability of the latter instrument in reproducing the radiance field. All data are given for the same sky planes at, or near (due to change in sun position during measurements), the sun and sun-normal zenith planes. In Figs. 7–9 HHCRM data (taken with sun zenith of 18 degrees and azimuth of 142 degrees) are shown for the sun (a) and sun-normal (b) zenith planes and compared with RADS data taken just before and after the HHCRM measurements. Comparisons are affected by the error in collocating the azimuth planes of the two instruments (less than 3 degrees) and the change in sun zenith and azimuth angles (about 2 and 9 degrees respectively) between beginning and conclusion of a measurement set. In the

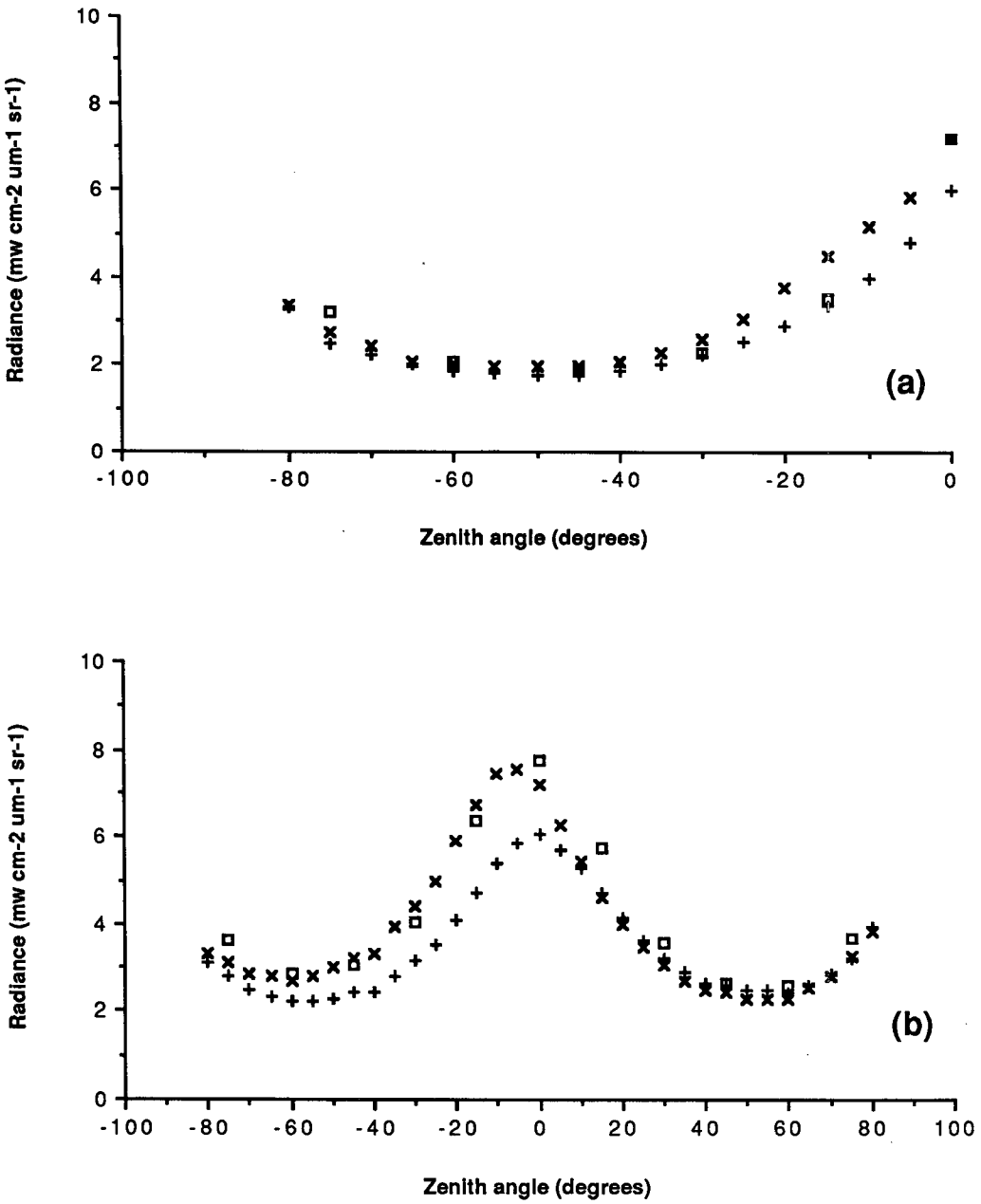

FIG. 9. Comparison between RADS data (×, +) and HHCRM data (□) taken at 600 nm and 611 nm central wavelengths respectively, in the sun plane (a) and in the sun-normal plane (b).

sun zenith plane, the radiance distribution is not sensitive to small variations in azimuth and RADS and HHCRM data agree quite well in all the cases. In the RADS measurements an occulter shadows the direct solar irradiance, as this is several decades higher than the maximum input value of the camera, and moreover causes undesired scattering in the optics. The occulter used in our measurements blocks the sky radiance at all zenith angles in the direction of the solar azimuth, and because of this the graphs in Figs. 7–9 (a) do not extend in this direction. In the sun-normal plane, the radiance distribution is very sensitive to azimuth angle, and data show more variation (the error in collocating the azimuth planes of the two instruments is estimated to be on the order of 3 degrees). In general, though, good agreement is found between measurements taken with the two instruments, thus experimentally validating the calibration procedure used for RADS.

The fisheye camera system, compared with traditional instruments (such as the HHCRM), excels as a method of obtaining radiance information for the complete distribution over an hemisphere. Figure 10

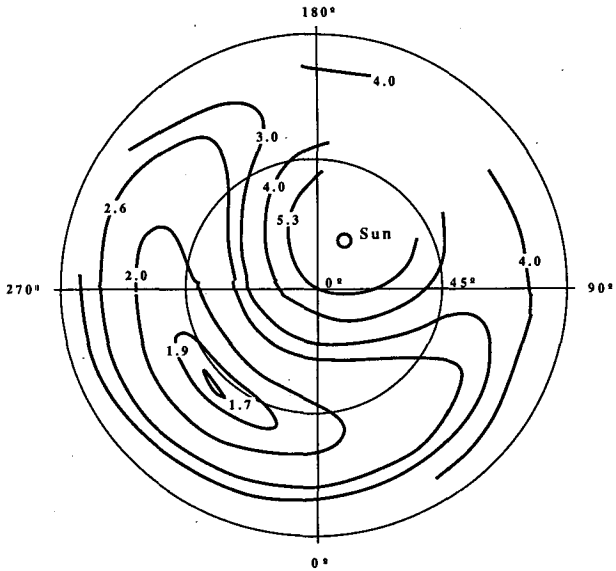

FIG. 10. Contour plot of radiances (units of mw cm^{-2} um^{-1} sr^{-1}) obtained from data taken with RADS at 600 nm (after Zibordi and Voss 1988).

shows a contour plot derived from a calibrated image obtained with channel 3 of RADS. The undefined area corresponds to the circumsolar zone shadowed by the occulter.

5. Conclusion

The calibration techniques applied to a fisheye electro-optic camera system have been described and validated through comparisons with measurements taken by a standard sky radiometer. Results demonstrate the capability of the camera to give data with good accuracy and illustrate its usefulness in performing spectral radiance distribution measurements with a high geometrical resolution, in the short time required for a changing light field.

Acknowledgments. RADS was developed at the Visibility Laboratory of the Scripps Institution of Oceanography and supported by the Office of Naval Research under contract N00014-85-C-0730. This work has been supported by the U.S. Office of Naval Research under this same contract and N00014-85-K-0005, and with the additional support of the Italian National Council of Research. Preliminary design work on the filter changer was supported by the U.S. Air Force Geophysics Laboratory contract F19628-84-K-0047. We would also like to thank Ms. Janet Shields and Mr. Roswell Austin for their critical review of the manuscript.

REFERENCES

Babey, S. K., J. S. Murphree, E. P. King, L. L. Cogger and C. D. Anger, 1986: Intensified charge-coupled-device imager for auroral studies. *Opt. Eng.*, **25**, 1149–1154.

Boileau, A. R., and J. I. Gordon, 1966: Atmospheric properties and reflectances of ocean water and other surfaces for a low sun. *Appl. Opt.*, **5**, 803–813.

Deering, D. W., and T. F. Eck, 1987: Atmospheric optical depth effects on angular anisotropy of plant canopy reflectance. *Int. J. Remote Sens.*, **8**, 893–916.

Miyamoto, K., 1964: Fisheye lens. *J. Opt. Soc. Amer.*, **54**, 1060–1061.

Plass, G. N., and G. W. Kattawar, 1970: Polarization of the radiation reflected and transmitted by the earth's atmosphere. *Appl. Opt.*, **9**, 1122–1130.

Sims, G. R., and M. B. Denton, 1987: Characterization of a charge-injection-device camera system as a multichannel spectroscopic detector. *Opt. Eng.*, **26**, 1008–1019.

Slater, P. N., 1980: Remote sensing. *Optics and Optical Aspects,* Addison-Wesley, 116–119.

Smith, R. C., 1974: Structure of solar radiation in the upper layers of the sea. *Optical Aspects of Oceanography,* N. G. Jerlov and E. S. Nielsen, Eds., Academic Press, 95–119.

Tyler, J. E., 1960: Observed and computed path radiance in the underwater light field. *Marine Res.*, **18**, 157–167.

Voss, K. J., 1989: An underwater electro-optic radiance distribution camera system. *Opt. Eng.*, **28**, 241–247.

Waterman, H., 1955: Polarization of scattered sunlight in deep water. *Marine and Biology in Oceanography.* Pergamon Press, 426–434.

Wilson, W., 1979: Measurements of atmospheric transmittance in a maritime environment. *Atmospheric Effects on Radiative Transfer,* SPIE Vol. 195, 153–159.

Zibordi, G., and K. J. Voss, 1988: Geometrical and spectral distribution of sky radiance: comparison between simulations and field measurements. *Remote Sens. Environ.* (in press)